Late Eocene-early Oligocene paleoenvironmental changes recorded at Lühe, Yunnan, southwestern China

Vittoria Lauretano[1], Caitlyn R. Witkowski[1*], Alex Farnsworth[2], Shu-Feng Li[3], Shihu Li[4,5], Jan Peter Mayser[1], B. David A. Naafs[1], Robert A. Spicer[3,6], Tao Su[3], He Tang[3,7], Zhekun Zhou[3], Paul J. Valdes[2], Richard D. Pancost[1]

[1]Schools of Chemistry and Earth Sciences, and Cabot Institute, University of Bristol, BS8 1TS

[2]School of Geographical Sciences and Cabot Institute, University of Bristol, Bristol, BS8 1SS, UK

[3]CAS Key Laboratory of Tropical Forest Ecology, Xishuangbanna Tropical Botanical Garden, Chinese Academy of Sciences, Mengla 666303, China

[4]State Key Laboratory of Lithospheric Evolution, Institute of Geology and Geophysics, Chinese Academy of Sciences, Beijing 100029, China

[5]Lancaster Environment Centre, Lancaster University, LA1 4YQ, Lancaster, UK

[6]School of Environment, Earth and Ecosystem Sciences, The Open University, Walton Hall, Milton Keynes, MK7 6AA, UK

[7] State Key Laboratory of Isotope Geochemistry, Guangzhou Institute of Geochemistry, Chinese Academy of Sciences, Guangzhou 510640, China.

[*]Corresponding author: caitlyn.witkowski@bristol.ac.uk @caitwitkowski

Abstract

During the late Eocene to the early Oligocene, marine records document a globally congruent record of declining carbon dioxide concentrations, Antarctic icesheet growth, and associated reorganisation of the global climate system. In contrast, the few existing terrestrial records demonstrate high heterogeneity of environmental change and are difficult to reconcile with those of the oceanic realm. Global drivers for climatic change are particularly difficult to disentangle from regional ones, especially those caused by the complex tectonic evolution of the Tibetan region and its influence on the Asian monsoon system and vegetation. Here, we reconstruct the climatic and environmental history from the late Eocene into the early Oligocene at Lühe Basin, Yunnan, China, a key sedimentary repository along the SE margin of the Tibetan Plateau and an important region for assessing Asian monsoon changes. We investigate a 340-m long section via a multi-proxy approach and climate model simulations. The organic geochemical proxies, via *n*-alkanes, terpenoids, and hopanes, suggest that thermally immature sediments were deposited in a terrestrial flood plain basin that was primarily occupied by gymnosperms and angiosperms. Branched glycerol diakyl glycerol tetraethers indicate relatively stable temperatures (ca. 10 °C) throughout the section, including across the Eocene-Oligocene boundary. This temperature, cooler than the modern-day average for this site (ca. 15 °C), suggests that this area has not undergone significant uplift since the Oligocene. To further contextualize our data, we tested a suite of climate model simulations with varying pCO_2, paleogeography, and Tibetan topography across the Eocene-Oligocene boundary. This data-model comparison suggests that a response to regional factors might explain the absence of a pronounced cooling at Lühe across the Eocene-Oligocene boundary, supporting the emerging picture that the global expression of the EOT in terrestrial environments is more complex than indicated by the marine record.

Keywords: brGDGTs, terrestrial temperature, biomarker, Tibet, E-O transition, monsoon

Highlights:

- Depositional environment primarily terrestrial flood plain basin, with gymnosperms
- Relatively stable mean annual temperatures (ca. 10 °C) across EOT
- Eastern Tibet at its current height since at least the EOT
- Data-model comparison suggests regional factors may explain lack of cooling at EOT
- Global expression of the EOT in terrestrial environments is highly heterogenous

1. Introduction

From the late Eocene to the early Oligocene, Earth's climate transitioned from an ice-free warmhouse world to icehouse world with large continental ice sheets. In deep-sea benthic records, the long-term cooling trend that started in the late Eocene reached its maximum late Paleogene expression across the Eocene-Oligocene Transition (EOT ~34 Ma, e.g., Westerhold et al., 2020 and references therein), as recorded by a rapid increase in the $\delta^{18}O$ of benthic foraminifera that reflect cooling and the onset of widespread Antarctic glaciation. The main hypothesis attributes this transition to the long-term drawdown of atmospheric pCO_2 (Anagnostou et al., 2016; DeConto and Pollard, 2003; Lauretano et al., 2021), although others invoke the main driver as the establishment of the Antarctic Circumpolar Current (ACC) and reorganization of oceanic gateways that led to the thermal isolation of Antarctica (e.g., Bijl et al., 2013). The cooler conditions persisted through most of the Oligocene until at least 26 Ma, when deep-sea benthic records indicate a warming phase and reduced extent of the Antarctic ice sheets (Westerhold et al., 2020).

While marine records are well-documented across this period, less is known about the terrestrial expression of Eocene-to-Oligocene; the relatively few available terrestrial records indicate strong heterogeneity of responses in environmental change (e.g., Hren et al., 2013; Lauretano et al., 2021; Sheldon et al., 2016, 2012; Zanazzi et al., 2007). Even fewer records document changes occurring in the Asian continental interior across this critical climatic transition; here, the few available terrestrial records indicate regional aridification and cooling in NE Tibet (e.g., Zanazzi et al., 2007). For example, the radiometrically dated plant-fossil assemblages from the SE margin of Tibet reveal a composition change from sub-tropical/warm-temperate to cool-temperate across the late Eocene into the early Oligocene (Su et al., 2019b), possibly reflecting either secular climate change, the uplift of this area to its modern-day elevation, or a combination of both.

The complex topographic and tectonic evolution of Tibet during the Cenozoic (Spicer et al., 2020a, and references therein), following the India-Eurasia continental collision during the early Paleogene, is likely linked with regional climatic responses, especially in the Asian monsoon system (Farnsworth et al., 2019; Huber and Goldner, 2012). In addition to regional climatic changes, Asia was also characterized by heterogenious and regionally complex changes in biodiversity (e.g., Li et al., 2021). For example, the changing Tibetan landscape likely profoundly impacted Yunnan, one of Asia’s biodiversity hotspots, situated in southwestern China along the SE Tibetan margin (Li et al., 2020; Spicer et al., 2020a). However, the lack of other (well-dated) sections has hindered attempts to correlate these interior locations to the global Cenozoic climate trends extrapolated from marine records. Reconstructing the climatic history of sedimentary basins along the margin of Tibet, in the context of a detailed temporal framework, is crucial to understanding the connection between topographic relief and climate, their influence on the Asian monsoon system, and the link to global climate.

Although modelling and paleobotanical efforts have recently been made to better constrain late Paleogene climate and biota throughout the Tibetan region (Su et al., 2020, 2019a), few have used quantitative organic geochemical proxies. Here, we reconstruct the environment in the Lühe basin (Yunnan province, China) by first determining the thermal maturity of the organic matter via e.g., bacteria-derived hopanes and eukaryote-derived *n*-alkanes, and then teasing out the organic sources and environmental conditions through gymnosperm-derived diterpenoids, angiosperm-derived triterpenoids, and eukaryote-derived *n*-alkanes. We then reconstruct mean annual temperatures using branched glycerol dialkyl glycerol tetraethers (brGDGTs), membrane-spanning lipids likely synthesized by bacteria and widely used as paleothermometers. Using these proxies, we present a new environmental and temperature reconstruction from the Lühe coalmine section spanning the latest Eocene to the early Oligocene, as constrained by magneto- and radio-isotopic dating. Moreover, we compare our results with climate model simulations through model-data comparison to assess the regional impact of secular climate change through the Eocene-Oligocene (E-O) transition.

2. Materials and Methods

2.1 Geological context

The Lühe Basin is located in Nanhua County along the southern side of the Chuxiong fault, situated in central Yunnan Province, southwestern China (Fig. 1). As an understudied midway point between southern China and Tibetan, the Lühe Basin is considered a key location to reconstruct structural and paleoclimatic evolution along the SE margin of Tibet (Li et al., 2020).

Sediment in the Lühe basin was initially assigned to the late Miocene based on palynological and floral evidence, as well as regional stratigraphic correlations (Xu et al., 2008; Zhang et al., 2007). However, U-Pb zircon ages from volcanic ashes in Lühe town indicated an age of ~33 Ma (Linnemann et al., 2018), backdating at least part of the Lühe Basin to the earliest Oligocene. More recently, Li et al. (2020) further constrained this age by providing a new magneto- and radio-isotopic framework for the sedimentary succession exposed in the close-by Lühe coalmine (25°10′N, 101°22′E; Fig. 1). The new $^{40}Ar/^{39}Ar$ dating of feldspars within volcanic ashes exposed in the lower portion of the coalmine provides an age of 33.32 ± 0.36 Ma, in agreement with zircon-derived U/Pb ages from the Lühe town section, ~2.6 Km southeast of the Lühe coalmine (Linnemann et al., 2018).

Magnetostratigraphic interpretation of the Lühe coalmine constrains this succession to span Chrons C15n and C9n (ca. 35-26 Ma, Gradstein, 2012), with an average sedimentation rate of ~48 cm/kyr, consistent with the rates found in other basins around the Tibetan Plateau (Li et al., 2020). The Lühe coalmine succession comprises alternations of organic-rich marls, mudstones, sandstones, and lignite (immature fossilised peat) deposits (Fig. 1). A thick coal interval (~4 m) at ~50 m from base of the coal mine contains 11 volcanic ash layers, some of which were used for dating. The measured ~340-m thick profile was logged in 2018 along the SE margin of the exposed Lühe coalmine and is stratigraphically correlated with that of Li et al. (2020) (Fig.1).

2.2 Organic geochemistry

2.2.1 Sample preparation

A total of 56 samples were analysed for organic geochemistry in order to determine the preservation state of the sediments, the paleoclimatic conditions, and the paleovegetation. Samples were extracted using a microwave-assisted extraction system with dichloromethane (DCM) and methanol (MeOH) (9:1 v/v). The resulting total lipid extract (TLE) was eluted with alumina column chromatography into an apolar fraction using hexane:DCM (9:1 v/v) and a polar fraction using DCM:MeOH (1:2 v/v). Apolar fractions were then analyzed via GC-MS and polar fractions were analyzed via HPLC-MS. For a detailed description of the analytical proceedures, see Supplementary Material.

2.2.2 Indices for thermal maturity

The apolar fraction contains compounds predominantly derived from plant, algal, and bacterial communities. Bacteria-derived hopanes and eukaryote--derived *n*-alkanes were used to assess the degree of thermal maturity of the organic matter preserved in the sediments, as high thermal maturity may bias the preservation of organic matter and thus the fidelity of our reconstructions. Here we calculated the stereochemistry of the C_{31} hopane at the C–17 and –21 positions, expressed as the ββ / (ββ + αβ + βα) ratio, which decreases with increasing thermal maturity (Fig. 2). To provide supplementary constraints on the thermal maturity, we also calculated the carbon preference index (CPI), which measures the odd-over-even preference of mid- and long-chain *n*-alkanes. Odd-carbon-number *n*-alkanes are preferentially biosynthesised, meaning biological distributions have high CPIs; this CPI decreases with both degradation and thermal maturity. Here, CPI is calculated as (Σodd (C_{21}“-“C_{33}) + Σodd (C_{23}“-“C_{35})) / (2 × Σeven (C_{22}“-“C_{34})) to avoid overestimation of the odd-over-even preference (Marzi et al., 1993).

2.2.3 Indices for vegetation and environmental reconstructions

Eukaryote-derived compounds (i.e., *n*-alkanes, diterpenoids, triterpenoids) were used to identify vegetation and environmental conditions. The average chain length (ACL) of *n*-

alkanes can be indicative of the organic matter source and is calculated as ACL = $\Sigma(C_n \times n)$ / $\Sigma(C_n)$ (Eglinton and Hamilton, 1967), here based on odd *n*-alkane chain-lengths from C_{21} through C_{33}. The P-aqueous ratio (P_{aq}, calculated as $P_{aq} = (C_{23} + C_{25}) / (C_{23} + C_{25} + C_{29} + C_{31})$, Ficken et al., 2000) and the $C_{23} / (C_{23} + C_{31})$ index (Nott et al., 2000) are generally associated with wetland conditions, given that C_{23} and C_{25} *n*-alkanes are produced by *Sphagnum* mosses and some submerged vascular macrophytes but are generally absent in higher plants. CPI, as described in 2.2.2, was used as supplementary information for interpreting terrestrial input.

2.2.4 brGDGT indices for MAAT and pH

The polar fractions contained brGDGTs, membrane-spanning lipid biomarkers used to reconstruct mean annual air temperature (MAAT) and pH (De Jonge et al., 2014; Naafs et al., 2017a, 2017b; Weijers et al., 2007). Although impossible to rule out, seasonal temperature fluctuation is not considered to affect the temperature signal since 1) there is no apparent seasonal pattern in mid-latitude soils (Weijers et al., 2011); and 2) in the case of peat settings, bacterial production is concentrated at depths below the water table, where seasonal variability converges in mean annual temperatures (Naafs et al., 2017b).

The degree of methylation of branched tetraether (MBT) is correlated with MAAT, based on the distribution of brGDGTs in mineral soils (Weijers et al., 2007). This was later updated by De Jonge et al. (2014), who developed two new temperature calibrations, one based on the temperature-dependence of 5-methyl brGDGTs alone (MBT'_{5me}), that excludes the possibly pH-dependant 6-methyl brGDGTs:

$$MBT'_{5me} = (Ia + Ib + Ic)/ (Ia + Ib + Ic + IIa + IIb + IIc + IIIa) \text{ (Fig. S1)}$$

$$MAT\ (°C) = -8.57 + 31.45 \times MBT'_{5me} \text{ (n=231, R2= 0.64, RSME= 4.9 °C)}$$

and one based on multiple linear regression (MAT_{mr}), considering specific 5-methyl brGDGTs:

$$MAT_{mr}\ (°C) = 717 + 17.1 \times Ia + 25.9 \times Ib + 34.4 \times Ic - 28.6 \times IIa \text{ (n=231, } R^2 = 0.67, \text{ RSME= 4.7 °C)}$$

Further revision of the available global soil brGDGT data excludes from the compilation 6-methyl dominated brGDGTs from arid and/or alkaline soils (Naafs et al., 2017a), leading to

$$MAAT_{soil} = 40.01 \times MBT'_{5me} - 15.25 \ (n = 350, R^2 = 0.60, RMSE = 5.3\ °C).$$

The degree of cyclization of branched tetraethers (CBT) correlates with pH in mineral soils (Weijers et al., 2007). The CBT index was later revised into CBT' (De Jonge et al., 2014), including 6-methyl brGDGTs and improved the correlation with pH:

$$CBT' = {}^{10}\log\left[(Ic+IIa'+IIb'+IIc'+IIIa'+IIIb'+IIIc')/(Ia+IIa+IIIa)\right]$$

$$pH = 7.15 + 1.59 \times CBT', \ (n=221, R^2 = 0.85, RSME = 0.52)$$

Most work on brGDGTs is based on mineral soils, but brGDGTs are particularly abundant in peat deposits (Sinninghe Damsté et al., 2000; Naafs et al., 2019). The relationship between environmental parameters and the distribution of brGDGTs in peats led to the first peat-specific temperature and pH calibrations based on a global peat database (Naafs et al., 2017b). The relationship between MBT'_{5me} and MAAT is in this case expressed as:

$$MAAT_{peat}\ (°C) = 52.18 \times MBT'_{5me} - 23.05 \ (n = 96, R^2 = 0.76, RMSE = 4.7\ °C)$$

while the correlation between brGDGTs and pH is defined as:

$$CBT_{peat} = \log\left[(Ib+IIa'+IIb+IIb'+IIIa')/(Ia+IIa+IIIa)\right]$$

$$pH = 8.07 + 2.49 \times CBT_{peat}, \ (n=51, R^2 = 0.85, RSME = 0.8)$$

In this study, we applied and compared the soil MAT calibrations by De Jonge et al. (2014) and Naafs et al. (2017a), and the peat-specific calibration by Naafs et al. (2017b) (see results).

The Branched vs. Isoprenoidal Tetraether (BIT) index was used to indicate the relative input of terrestrial and marine organic matter, defined by (Hopmans et al., 2004) as:

$$BIT = (Ia+IIa+IIa'+IIIa+IIIa') / (Ia+IIa+IIa'+IIIa+IIIa' + Crenarchaeol).$$

In addition to bacterial brGDGTs (Fig. S1), this includes the isoprenoidal (iso)GDGT known as crenarchaeaol, which is produced by Thaumarchaeota and is especially abundant in marine settings.

2.3 Climate model simulations

Here, we utilised a suite of climate model simulations to assess the impact on Asian climate in the context decreasing atmospheric concentrations of carbon dioxide ($p\text{CO}_2$) and the formation of a Southern Hemisphere icesheet through the E-O transition. Using the late Eocene (Priabonian stage) and Oligocene (both Rupelian and Chattian stages) boundary conditions, we employed HadCM3BL-M2.1aD (Valdes et al., 2017), a fully coupled ocean-atmosphere and dynamic vegetation General Circulation Model (GCM) with a 3.75 x 2.5 latitude by longitude spatial grid (~300 km), 19 vertical levels in the atmosphere, and 20 vertical levels in the ocean. HadCM3BL-M2.1aD, a primary model of the IPCC AR3 to AR5 experiments, has shown spatio-temporal skill in reproducing the modern observed Asian monsoon and paleo-monsoon (Farnsworth et al., 2019), providing confidence in its thermodynamic and hydrologic response to perturbed forcing for the current region of interest.

Model boundary conditions (topography, bathymetry, and ice sheet configurations; at 0.5 x 0.5° resolution and downscaled to model resolution) for each geologic stage, Priabonian (~36 Ma), Rupelian (~31 Ma), and Messinian (~25 Ma), are provided by Getech Plc. Stage-specific solar luminosity was calculated using the methods of (Gough, 1981). $p\text{CO}_2$ values were prescribed at 1120 ppm for the Priabonian and 560 ppm for the Rupelian and Chattian, consistent with the Phanerozoic $p\text{CO}_2$ compilation of (Foster et al., 2017; Witkowski et al., 2018).

Each experiment was run for 12,422 model years to allow surface and deep ocean to reach equilibrium and to achieve a state with no net energy imbalance at the top of the atmosphere. This is fundamental as ocean circulation can take many thousands of model years to establish its equilibrium state, with a significant influence on the climate signal leading to a potentially erroneous state if not adequately spun-up (Farnsworth et al., 2019). Climate means are calculated from the last 100-years of each simulation. Time-varying latitude and longitude plate paleo-rotations are provided for the Lühe Basin for each stage to allow for accurate comparison within the model. The paleo-coordinates (21.1° N) for Lühe were calculated using the Getech plate model.

3 Results & Discussion

3.1 Thermal maturity of sediments

The apolar fractions were used to estimate thermal maturity (Figs. 2, 3). The C_{31} hopane configuration ratio of ββ / (ββ + αβ + βα) ranges from 0.0 to 0.7 (from high to low thermal maturity, respectively) with a mean of 0.4 ± 0.2 σ (Fig. 3A). Values are slightly lower in the bottom ~30 m of the section. Although variable, most values are over 0.3 and there is no consistent trend through the section. Instead, it appears that the organic matter is relatively immature with an admixture of mature, reworked organic matter in some low-TOC intervals. The CPI ranges from 1.9 to 9.4 with a mean of 4.9 ± 1.6 σ (Fig. 3B). These CPI values likewise suggest that these sediments are relatively immature, although the variation reflects the dynamic depositional environment.

3.2 Vegetation and environmental reconstruction

Throughout the section, the *n*-alkane distribution shows a strong odd-over-even preference (Fig. 3B), with a CPI ranging from 1.9 to 9.4 with a mean of 4.9 ± 1.6 σ, suggesting this is primarily terrestrial in origin. In most of these sediments, the apolar fractions are dominated by the C_{29} *n*-alkane, followed by a high abundance of the C_{27} and then C_{31} *n*-alkanes (Figs. 2A; 4), suggesting dominance of higher plants. The ACL ranges from 26.1 to 29.6 with a mean of 28.4 ± 0.6 σ (Fig. 3C). This relatively high CPI (Fig. 3B), high ACL (Fig. 3C), and dominance of the C_{29} *n*-alkane (Fig. 2A, 4) suggests that the vegetation at this site was likely dominated by woody angiosperms and gymnosperms. More specifically, the ACL of 28.4 is more likely associated with deciduous rather than evergreen angiosperms.

Several samples also contained diterpenoids and triterpenoids (Fig. 2A), indicative of gymnosperms and angiosperms respectively, which may provide further insights into the type of vegetation at this site. Throughout the section, the abietane-based diterpenoids (18-

norbietane at 21.4 and 268.0 m, 18-norabieta-8,11,13-triene at 21.4 m, 10,18-bisnorabieta-5,7,9(10),11,13-pentaene at 21.4 m, and dehydroabietane at 228.5 and 268.0 m) are indicative of the Pinaceae family. The inclusion of the Pinaceae family in the vegetation is further supported by the presence of simonellite (228.5 and 268.0 m), a diterpene present in conifer resin. Evidence of conifers in the catchment area is further suggested by the presence of norpimarane at depths 21.4 and 268.0 m, which is particularly abundant in *Pinus*, *Larix*, and *Picea*. Several samples also contained triterpenoids, including tetramethyl-octahydrochrysene (22.4 m) and Des-A-lupane (40.7, 105.6, 289, 301.9 m), compounds synthesized by nearly all angiosperms. The more frequent abundance of diterpenoids-over-triterpenoids in these sediments suggest that this environment was likely dominated by gymnosperms with some angiosperms, although it should be noted that taphonomy processes can skew plant preservation and associated biomarker distributions.

Our biomarker-based vegetation reconstruction is consistent with the plant fossil assemblage recovered from the nearby Lühe town section, which is age-correlated with the basal portion of our coal mine section. At the town section, previous work identified 38 floral genera, assigned to 26 angiosperms, 6 gymnosperms, and 4 ferns (Tang et al., 2020). Analyses of the paleo-vegetation reveal that trees and shrubs dominated most of the section, as also indicated by tree stumps, fallen logs, and branches present throughout the section (Yi et al., 2003). The ACL values are also supported by palynological results, which indicate a temperate deciduous broadleaved flora mixed with some evergreen broadleaved taxa and conifers (Tang et al., 2020). Evergreen oaks (*Quercus*) and alder (*Alnus*) were identified, and palynomorphs were dominated by *Quercoidites* (43%), *Titricolpites* (12.5%), *Pinuspollenites* (6.93%), and *Piceapollis* (0–18.6%). These are not necessarily representative of *in-situ* assemblages given that pollen might have been blown/washed into the basin from the surrounding (and possibly higher) areas but are consistent with the biomarker assemblages in our samples.

The P_{aq} ranges from 0.0 to 0.9 (terrestrial to aquatic, respectively). Most values range between 0.2 and 0.5 with a mean of 0.4 ± 0.2 σ. A P_{aq} < 0.23 is considered indicative of terrestrial plant waxes, while > 0.48 is common for submerged and floating macrophytes (Ficken et al., 2000). Because our P_{aq} sits in the middle of these ranges, this may have been a wet terrestrial environment, like a floodplain. This is further supported by the sedimentary succession (Fig. 3) and high abundance of *Equisetum* cf. *pratense* seen in the coalmine section (Zhang et al., 2007), which is indicative of wet terrestrial environments. However, the variation is again representative of a dynamic depositional environment.

Notably, the apolar distribution of two sediment depths (26.7 and 58.5 m) appear different from the rest of the section (Fig. 3B). These two sediment depths lie more than 2σ outside the ACL and P_{aq} distribution (Fig. 3C-D), with the ACLs being particularly low (25.2 and 25.3 respectively, relative to the average of 27.6 ± 0.8 σ) and the P_{aq} being particularly high (0.9 and 0.8 respectively, relative to the average of 0.3 ± 0.2 σ). Although these two sediment depths still contain *n*-alkanes with a strong odd-over-even preference and long chain-lengths associated with higher plants (i.e., C_{27}, C_{29}, and C_{31}), they show a clear C_{23} and C_{25} dominance, which is considered a robust signature for either *Sphagnum* peat mosses (Nott et al., 2000) or aquatic plants (Ficken et al., 2000). Therefore, these two outlier horizons may represent swampy environments or even open water conditions. Interbedded lignites found throughout the section further confirm that this was (at times) a peat-forming environment. This environment is consistent with a riverine floodplain, as also supported by the presence of sedimentary structures of river channels and sedimentological evidence of intervals of water-logging conditions.

Taken together, our biomarker results are compatible with a terrestrial environment (likely a flood plain) with organic-rich soils derived from swamps, colluvium, occasional peat-forming, and wet areas. We do see evidence for abundant terrestrial biomarkers (e.g., leaf waxes, terpenoids indicative of woody gymnosperms and angiosperms, and soil bacterial lipids) and we do not see evidence for aquatic inputs (e.g., low CPI, low ACL, and strong presence of algal biomarkers). The specific higher plant biomarkers are also consistent with this area being covered in deciduous and evergreen broad-leaved mixed forests, as observed in the nearby Lühe town section (Tang et al., 2020).

3.3 Climate reconstruction using GDGT indices

Lithologies in the Lühe coalmine section vary; lithologies include sands, mudstones, and coal/lignite layers, and are interbedded with fossil remains of wood (logs and branches) and leaves (Fig. 3). Such lithological variability is indicative of a dynamic paleoenvironment, likely a flood plain, where deposition of swamp-derived organic-rich soils were interspersed with colluvium, occasional peat mire, and shallow stagnant environments (Xu et al., 2008). This dynamic environment poses a challenge for the application of a univocal brGDGT paleothermometer calibration. Therefore, we rely on a series of characteristics stemming from field observations, TOC (wt%) data, and organic geochemical analyses to constrain the type of lithology and paleoenvironment, and then apply three different brGDGT-temperature calibrations (Fig. 5).

Most sediments (n = 46) have a TOC (wt%) ranging between 0.1–23 % with the majority < 3% (Fig. 5), consisting of the lithologies categorised from mudstone to silty sandstones. The remaining sediments (n=10) have TOC (wt%) ranging between 40–63 %; these high TOC ranges are indicative of organic-rich environments, consistent with the presence of coal layers identified in the stratigraphy. Samples from sand lithologies were tested and excluded from the sample set as they did not yield sufficient organic matter for analysis (Fig. 5).

Of all samples analysed (n = 56), 38 yielded sufficient brGDGTs for paleotemperature estimates (Fig. 5). For samples with TOC (wt%) <23 % (n = 33), we cannot further constrain the type of paleoenvironment and/or the source of bacterial production (e.g., lacustrine vs soil). Thus, we apply both the MAT and pH soil calibration by De Jonge et al. (2014) and MAT soil calibration of Naafs et al. (2017a) (Fig. 5). For the samples with TOC (wt%) >23 % (n = 5), identified as lignites/coals, we further apply the peat-specific temperature and pH calibration by Naafs et al (2017b) (Fig. 5).

MAAT values range from 4.9 to 14.7 °C (± 4.9 °C) using the de Jonge et al. (2014) soil calibration and between 3.8 and 14.4 °C (± 5.3 °C) using the Naafs et al. (2017a) soil calibration, with average temperatures of ca. 9-10 °C. The Naafs et al. (2017b) peat-specific calibration yielded MAAT values from 5.3 to 15.4 °C (± 4.7 °C) for the five lignite samples, with warmer values at the top of the section. Temperature estimates throughout the section show some variability, possibly due to the mixing in the rapidly changing environments. However, the overall trend, highlighted by the 2-point moving average (Fig. 5), shows that average temperatures remained rather stable throughout (regardless of calibration), with only a slight warming towards the top of the section.

pH values range between 3 and 6, with an average value of 4, and show increased variability in the upper interval of the section where pH increases (Fig. 5; 310-340 m). These values are consistent with an acidic peat environment. The BIT index is consistently above 0.87 (Fig. 5), indicating a dominance of brGDGTs over crenarchaeol and consistent with a terrestrial-dominated source of organic matter throughout the section (Hopmans et al., 2004).

Mean annual temperatures across this section are consistent with a temperate climate, which persisted without major fluctuations from the end of the Eocene through to the early Oligocene. We do not find evidence of significant cooling across the Eocene-Oligocene transition, which would have been preserved within the first 60 m of the section, based on radio-isotopic ages (Li et al., 2020). This could be due to imprecise age constraints, or to the presence of a hiatus in the sequence, although the radio-isotopic datum in the lower portion of the section and the magnetostratigraphic interpretation of this section by Li et al. (2020) do not seem to support these hypotheses. Alternatively, our reconstruction shows that climate at Lühe remained relatively stable from the late Eocene to the early Oligocene and it did not experience the cooling observed at other terrestrial locations across the globe during the EOT (e.g., Zanazzi et al., 2007).

Our results fit with the emerging picture that the global expression of the EOT in terrestrial environments is highly heterogenous (e.g., Hren et al., 2013; Lauretano et al., 2021; Sheldon et al., 2016; Zanazzi et al., 2007). Terrestrial temperature records across this interval are derived from a variety of qualitative and quantitative proxies (e.g., paleobotanical, palynological, geochemical). Vegetation records provide the most extensive global dataset of changes across the EOT and generally show a variety of responses, partly influenced by local/regional factors and changes in precipitation. Northern hemisphere geochemical records also depict a range of different responses, with paleosol records from North America generally indicating no change or a ~2-3 °C cooling (Retallack, 2007) but also, for example, a more dramatic ~8 °C temperature drop across the transition, as reconstructed by fossil teeth isotopic data (Zanazzi et al., 2007). In contrast, floral assemblages from the same region show a more protracted cooling from the early into the middle Oligocene (Retallack et al., 2004). Meanwhile, clumped isotope data from a freshwater gastropod shell from the Hampshire Basin (Isle of Wight, UK) indicate a 4-6 °C cooling from warm late Eocene estimates to the early Oligocene (Hren et al., 2013), while paleosol estimates from the Ebro Basin (Spain) suggest that temperature remained unvaried during this time (Sheldon et al., 2012). The response in southern hemisphere terrestrial temperatures vary, as well. Floral and isotopic records from Argentina indicate a ‘quasi-static’ climate across the Eocene and Oligocene (Kohn et al., 2015), but more recent data from volcanic glass stable hydrogen isotopes suggest that a 5 °C cooling occurred across this the EOT (Colwyn and Hren, 2019). Evidence of cooling across the EOT is also reported in a peat-specific lignite record from SE Australia, showing an average cooling of 2.4 °C from the late Eocene to the earliest Oligocene, coeval with a shift toward cooler species in the palynological record from the same facies (Lauretano et al., 2021).

With terrestrial temperature records presenting a rather heterogenous picture of the change at the EOT, whereas marine reconstructions consistently suggest a global average cooling of about 2.5 °C in sea-surface and deep-sea temperatures (Hutchinson et al., 2021). While we highlight that a relatively muted cooling of <1-2 °C might be difficult to detect in our proxy records, which are better suited for greater temperature oscillations (Naafs et al., 2017b), the results from this section represent one more puzzle piece in the terrestrial expression of the EOT and the possible influence of local factors on this response.

Finally, our results suggest that during this time, this intramountain basin likely consisted of a flood plain, hosting local swamps, colluvium, and occasional peat mires, as well as shallow submerged areas, dominated by terrestrial inputs. Modern-day mean annual temperatures in this area are of ca. 14.4-15.4 °C (http://data.cma.cn/en), indicating that this location was most likely already at least its present-day elevation during the early Oligocene, supporting the hypothesis that local uplift had already taken place at this time (Spicer et al., 2020a).

3.4 Climate model results

We employed a fully coupled atmosphere-ocean GCM with a range of perturbed Priabonian and Chattian boundary conditions to investigate potential mechanisms for our temperature proxy results. We tested the effects of different parameters on temperature and precipitation in this region (Table 1) across the E-O boundary and explore whether it was sensitive to a drawdown in $p\mathrm{CO_2}$ and the concurrent development of an Antarctic icesheet. Moreover, we compare our results with modelled temperature and precipitation responses under Chattian boundary conditions to test for Oligocene conditions with no additional site elevation or latitudinal changes during this time.

Firstly, we tested the impact of changing boundary conditions on the broader Asian region (0°N-60°N, 60°E-120°E), as seen in Table 1, considering changes in $p\mathrm{CO_2}$, global paleogeography, and the site elevation as variables across the E-O boundary. For the regional impact, a decrease from 4x to 2x pre-industrial $p\mathrm{CO_2}$ across the E-O boundary results in regional temperatures cooling by ~6 °C, regardless of topographic changes of the Tibetan Plateau (valley, plateau, or valley to plateau; Table 1, simulations 1-3). When assuming no change in pCO_2, global changes in paleogeography from a Priabonian to Chattian configuration produce a reduced impact on the climate of Asia, with a slight increase in MAT of 1.5 °C (Table 1, simulations 4-6). This is the result of regional changes to gateways, including the retreat of the Paratethys sea and the formation of Antarctic ice sheets. In all simulations including a change at the E-O boundary, MAP is similarly affected, increasing by ca. 150-200 mm/yr but this does not significantly vary amongst different topographic configurations.

As our section spans to the late Oligocene, we also compare our proxy results with model estimates calculated under Chattian boundary conditions. Under 2x pre-industrial pCO_2, the model reproduces an MAT of ~19 °C ± 0.4, for either a Tibetan topography with a 2.5-km valley or a 4.5-km plateau (Table 2) with seasonal changes varying from a cold-month mean temperature (CMMT) of ~12 °C to a warm-month mean temperature (WMMT) of 24 °C. These average estimates, although warmer than what we observe in our record, are still within error of the values we observe in the top interval of our proxy record (15 °C ± 4.7). The cooler temperatures shown by our proxy record could be due to the inclusion of organic matter from a wider catchment area in our biomarker data, including material washed in the basin from higher elevation surrounding the flood plain. This is compatible with the presence of sediment indicative of colluvium (fine mudstones, sandy beds) and the rich assemblages represented in the apolar fraction. The palynological results also suggested some conifers such as *Abies*, *Picea* and *Pinus*, may transferred from high elevation mountains nearby. However, despite being sparse, our lignite-based peat-specific MAAT estimates represent in-situ production and are largely in agreement with the other calibrations applied. Therefore, we are confident that our estimates provide a satisfying picture of the average temperatures at this location.

3.5 The evolution of the Tibetan region and Eocene/Oligocene climate

Based on our proxy data and model simulations, we note several possible places of agreement. Our GDGT-based temperatures suggest that there is minimal change across the section, with some potential warming towards the top of the section. Terrestrial temperature records, albeit sparse, suggest a more gradual pCO_2 decline across the Eocene to the earliest Oligocene than marine records, and a less pronounced response at the E-O boundary. This is consistent with marine geochemical proxies, including boron isotope ($\delta^{11}B$) records, that show that the decline in pCO_2 occurred progressively from the middle to the late Eocene (Anagnostou et al., 2016) and culminated in a further two-stepped decline at the EOT. Marine records generally suggest a pCO_2 decline from 1000 ppm in the Priabonian setting to 700 ppm during the Rupelian (Hutchinson et al., 2021), while stomatal records, for example, suggest pCO_2 values drop from 630 ppm in the late middle Eocene to ca. 365 ppm in the late Eocene, just prior to the EOT (Steinthorsdottir et al., 2016). It is worth noting that CO_2-forced GCM and dynamic ice-sheet model experiments reproduce a threshold for glaciation at around 780 ppm (DeConto and Pollard, 2003), from which a relatively small drop in pCO_2 would have been sufficient to initiate ice-sheet dynamics.

Assuming that the stratigraphy at this site does encompass the E-O boundary, the temperature response at Lühe might reflect paleogeographic changes rather than the effect of a rapid and large drop in pCO_2, as observed in the regional scale simulations (Table 1, simulations 4-6). The temperature decline of ~6 °C observed in the climate model simulations driven by a drawdown of pCO_2 are in line with the spread of available terrestrial proxy data (Hutchinson et al., 2021; Lauretano et al., 2021), and local factors might hinder the temperature response at our site. Additionally, the simulated drop in pCO_2 from 4x to 2x pre-industrial levels might overestimate the actual withdrawal of pCO_2 occurring across the E-O boundary, which might have been closer to a factor of 1.6x, based on the best fit in ensemble means (Foster et al., 2017; Hutchinson et al., 2021). A more gradual pCO_2 decline, as well as a smaller magnitude of drawdown, might explain a less pronounced response in terrestrial temperatures at our site.

Our brGDGT-based temperatures are also largely consistent with independent results from a Bioclimatic Analysis of the palynoflora (Tang et al., 2020) and Climate Leaf Analysis Multivariate Program (CLAMP) (Wolfe, 1993; Yang et al., 2011) which indicate an average mean annual temperature of 15.9 °C ± 2.36, CMMT of ~4.5 °C and WMMT of 26.9 °C for the leaf assemblage preserved in the Lühe town section. These results demonstrate a large mean annual range of temperatures, with likely infrequent winter frosting and warm summers. This would suggest a warm temperate climate rather than subtropical, with taxa with frost sensitive leaves prone to winter deciduousness. Precipitation during the growing season averaged 2250 mm ± 640 while precipitation during the three consecutive wettest months (3-WET) and the three consecutive driest months (3-DRY) range between 1110± 400 and 340± 98 mm respectively (Table 3). However, the overall precipitation is likely overestimated in CLAMP, and particularly for the dry months in warm climates, because water is not a limiting growth factor for plant growing near to aquatic depositional sites (Spicer et al., 2011).

Conclusions

We present a multi-proxy geochemical record to reconstruct paleoclimatic and paleoenvironmental conditions at Lühe, in central Yunnan, China, from the late Eocene-early Oligocene. Plant and bacteria-derived biomarkers indicate that this site on the south-eastern margin of Tibet represented a terrestrial flood plain environment, with occasionally submerged peat/swamp deposits. The abundance of terrestrial biomarkers indicative of woody gymnosperms and angiosperms is consistent with reconstructions of this area as covered by deciduous and evergreen broad-leaved forests, as observed for the nearby Lühe town section (Tang et al., 2020).

Mean annual temperatures, reconstructed using brGDGTs from bacterial lipids in soil and lignite samples, indicate average values of 9-10 °C, reaching maximum values of ~15 °C towards the top of the section. This suggests stable climatic conditions, with the possibility of a slight warming in the upper portion of this section. Using a fully coupled atmosphere-ocean GCM, we test a range of perturbed Priabonian and Chattian boundary conditions across the Eocene-Oligocene boundary for both the local and regional scale, including pCO_2, paleogeography, and varying Tibetan topography configurations. The muted response at our site might be due to the influence of local factors, as well as pointing to a smaller and more gradual drawdown of CO_2 across this transition, in line with results shown by GCM simulations (DeConto and Pollard, 2003; Hutchinson et al., 2021). Factors including regional and local response to paleogeographical conditions need further exploration, which can only be possible with additional records, as well as contributing to the effort of reconciling pCO_2 reconstructions from marine and terrestrial records.

Acknowledgements

This research was carried out with funding from the joint UK-China Project administered by the UK Natural Environment Research Council (NE/P013805/1) and the Natural Science Foundation of China Project (No. 41661134049, 41772026) and an XTBG Visiting Scholarship to RAS. ZZ thanks the Natural Science Foundation of China Project (No. 41661134049, 42072024) and SFL thanks the Natural Science Foundation of China for the Project funding (No. 41772026). We thank NERC (Reference: CC010) and NEIF (www.isotopesuk.org) for funding and maintenance of the instrumentation used for this work and Dr F. Sgouridis at the University of Bristol for technical assistance. B.D.A.N. acknowledges funding through a Royal Society Tata University Research Fellowship. In addition, NERC (Reference: CC010) and NEIF (www.isotopesuk.org) are thanked for funding and maintenance of the GC-MS and HPLC-MS instrument used for this work.

References

Anagnostou, E., John, E.H., Edgar, K.M., Foster, G.L., Ridgwell, A., Inglis, G.N., Pancost, R.D., Lunt, D.J., Pearson, P.N., 2016. Changing atmospheric CO_2 concentration was the primary driver of early Cenozoic climate. Nature 533, 380–384. https://doi.org/10.1038/nature17423.

Bijl, P.K., Bendle, J.A.P., Bohaty, S.M., Pross, J., Schouten, S., Tauxe, L., Stickley, C.E., McKay, R.M., Rohl, U., Olney, M., Sluijs, A., Escutia, C., Brinkhuis, H., Klaus, A., Fehr, A., Williams, T., Carr, S.A., Dunbar, R.B., Gonzalez, J.J., Hayden, T.G., Iwai, M., Jimenez-Espejo, F.J., Katsuki, K., Kong, G.S., Nakai, M., Passchier, S., Pekar, S.F., Riesselman, C., Sakai, T., Shrivastava, P.K., Sugisaki, S., Tuo, S., van de Flierdt, T., Welsh, K., Yamane, M., Röhl, U., 2013. Eocene cooling linked to early flow across the Tasmanian Gateway. Proceedings of the National Academy of Sciences 110, 9645–9650. https://doi.org/10.1073/pnas.1220872110.

Colwyn, D.A., Hren, M.T., 2019. An abrupt decrease in Southern Hemisphere terrestrial temperature during the Eocene–Oligocene transition. Earth and Planetary Science Letters 512, 227–235. https://doi.org/10.1016/J.EPSL.2019.01.052.

de Jonge, C., Hopmans, E.C., Zell, C.I., Kim, J.-H., Schouten, S., Sinninghe Damsté, J.S., 2014. Occurrence and abundance of 6-methyl branched glycerol dialkyl glycerol tetraethers in soils: Implications for palaeoclimate reconstruction. Geochimica et Cosmochimica Acta 141, 97–112. https://doi.org/10.1016/j.gca.2014.06.013.

DeConto, R.M., Pollard, D., 2003. Rapid Cenozoic glaciation of Antarctica induced by declining atmospheric CO2. Nature 421, 245–249.

Dupont-Nivet, G., Krijgsman, W., Langereis, C.G., Abels, H.A., Dai, S., Fang, X., 2007. Tibetan plateau aridification linked to global cooling at the Eocene-Oligocene transition. Nature 445, 635–8. https://doi.org/10.1038/nature05516.

Eglinton, G., Hamilton, R.J., 1967. Leaf Epicuticular Waxes. Author: Geoffrey Eglinton and Richard J. Hamilton Published by: American Association for the Advancement of

Science Stable URL: http://www.jstor.org/stable/1721263. Science 156, 1322–1335. https://doi.org/DOI: 10.1126/science.156.3780.1322.

Farnsworth, A., Lunt, D.J., O’Brien, C.L., Foster, G.L., Inglis, G.N., Markwick, P., Pancost, R.D., Robinson, S.A., 2019. Climate Sensitivity on Geological Timescales Controlled by Nonlinear Feedbacks and Ocean Circulation. Geophysical Research Letters 46, 9880–9889. https://doi.org/10.1029/2019GL083574.

Farnsworth, Alex, Lunt, D.J., Robinson, S.A., Valdes, P.J., Roberts, W.H.G., Clift, P.D., Markwick, P., Su, T., Wrobel, N., Bragg, F., Kelland, S.J., Pancost, R.D., 2019. Past East Asian monsoon evolution controlled by paleogeography, not CO2. Science Advances 5, eaax1697. https://doi.org/10.1126/sciadv.aax1697.

Ficken, K.J., Li, B., Swain, D.L., Eglinton, G., 2000. An n-alkane proxy for the sedimentary input of submerged/floating freshwater aquatic macrophytes. Organic Geochemistry 31, 745–749. https://doi.org/10.1016/S0146-6380(00)00081-4.

Foster, G.L., Royer, D.L., Lunt, D.J., 2017. Future climate forcing potentially without precedent in the last 420 million years. Nature Communications 8, 1–8. https://doi.org/10.1038/ncomms14845.

Gough, D.O., 1981. Solar interior structure and luminosity variations. Solar Physics 74, 21–34. https://doi.org/10.1007/BF00151270.

Gradstein, F.M., 2012. Introduction, The Geologic Time Scale 2012. Felix M. Gradstein, James G. Ogg, Mark Schmitz and Gabi Ogg. https://doi.org/10.1016/B978-0-444-59425-9.00001-9.

Hopmans, E.C., Weijers, J.W.H.H., Schefuß, E., Herfort, L., Sinninghe Damsté, J.S., Schouten, S., 2004. A novel proxy for terrestrial organic matter in sediments based on branched and isoprenoid tetraether lipids. Earth and Planetary Science Letters 224, 107–116. https://doi.org/10.1016/j.epsl.2004.05.012.

Hren, M.T., Sheldon, N.D., Grimes, S.T., Collinson, M.E., Hooker, J.J., Bugler, M., Lohmann, K.C., 2013. Terrestrial cooling in Northern Europe during the Eocene-Oligocene transition. Proceedings of the National Academy of Sciences of the United States of America 110, 7562–7. https://doi.org/10.1073/pnas.1210930110.

Huber, M., Goldner, A., 2012. Eocene monsoons. Journal of Asian Earth Sciences 44, 3–23. https://doi.org/10.1016/j.jseaes.2011.09.014.

Hutchinson, D.K., Coxall, H.K., Lunt, D.J., Steinthorsdottir, M., De, A.M., Baatsen, M., Heydt, A. Von Der, Huber, M., Kennedy-Asser, A.T., Ladant, J.-B., Lear, C.H., Moraweck, K., Pearson, P.N., Pound, M.J., Salzmann, U., Scher, H.D., Sijp, W.P., Kasia, K.Ś., de Boer, A.M., Baatsen, M., von der Heydt, A., Huber, M., Kennedy-Asser, A.T., Kunzmann, L., Ladant, J.-B., Lear, C.H., Moraweck, K., Pearson, P.N., Piga, E., Pound, M.J., Salzmann, U., Scher, H.D., Sijp, W.P., nska, S., Wilson, P.A., Zhang, Z., 2021. The Eocene-Oligocene transition: a review of marine and terrestrial proxy data, models, and model-data comparisons 17, 269–315. https://doi.org/10.5194/cp-17-269-2021.

Kohn, M.J., Strömberg, C.A.E., Madden, R.H., Dunn, R.E., Evans, S., Palacios, A., Carlini, A.A., 2015. Quasi-static Eocene-Oligocene climate in Patagonia promotes slow faunal evolution and mid-Cenozoic global cooling. Palaeogeography, Palaeoclimatology, Palaeoecology 435, 24–37. https://doi.org/10.1016/j.palaeo.2015.05.028.

Lauretano, V., Kennedy-Asser, A.T., Korasidis, V.A., Wallace, M.W., Valdes, P.J., Lunt, D.J., Pancost, R.D., Naafs, B.D.A., 2021. Eocene to Oligocene terrestrial Southern Hemisphere cooling caused by declining pCO2. Nat. Geosci. https://doi.org/10.1038/s41561-021-00788-z.

Li, S., Su, T., Spicer, R.A., Xu, C., Sherlock, S., Halton, A., Hoke, G., Tian, Y., Zhang, S., Zhou, Z., Deng, C., Zhu, R., 2020. Oligocene Deformation of the Chuandian Terrane in the SE Margin of the Tibetan Plateau Related to the Extrusion of Indochina. Tectonics 39, 1–17. https://doi.org/10.1029/2019TC005974.

Li, S.F., Valdes, P.J., Farnsworth, A., Davies-Barnard, T., Su, T., Lunt, D.J., Spicer, R.A., Liu, J., Deng, W.Y.D., Huang, J., Tang, H., Ridgwell, A., Chen, L.L., Zhou, Z.K., 2021. Orographic evolution of northern Tibet shaped vegetation and plant diversity in eastern Asia. Science Advances 7, 7741–7768. https://doi.org/10.1126/sciadv.abc7741.

Linnemann, U., Su, T., Kunzmann, L., Spicer, R.A., Ding, W.N., Spicer, T.E.V., Zieger, J., Hofmann, M., Moraweck, K., Gärtner, A., Gerdes, A., Marko, L., Zhang, S.T., Li, S.-H., Tang, H., Huang, J., Mulch, A., Mosbrugger, V., Zhou, Z.K., 2018. New U-Pb dates show a Paleogene origin for the modern Asian biodiversity hot spots. Geology 46, 3–6. https://doi.org/10.1130/G39693.1.

Marzi, R., Torkelson, B.E., Olson, R.K., 1993. A revised carbon preference index, Org. Geochem.

Naafs, B.D.A., Gallego-Sala, A.V., Inglis, G.N., Pancost, R.D., 2017a. Refining the global branched glycerol dialkyl glycerol tetraether (brGDGT) soil temperature calibration. Organic Geochemistry 106, 48–56. https://doi.org/10.1016/J.ORGGEOCHEM.2017.01.009

Naafs, B.D.A., Inglis, G.N., Blewett, J., McClymont, E.L.L., Lauretano, V., Xie, S., Evershed, R.P.P., Pancost, R.D.R.D., 2019. The potential of biomarker proxies to trace climate, vegetation, and biogeochemical processes in peat: A review. Global and Planetary Change 179, 57–79. https://doi.org/10.1016/j.gloplacha.2019.05.006.

Naafs, B.D.A., Inglis, G.N., Zheng, Y., Amesbury, M.J., Biester, H., Bindler, R., Blewett, J., Burrows, M.A., del Castillo Torres, D., Chambers, F.M., Cohen, A.D., Evershed, R.P., Feakins, S.J., Gałka, M., Gallego-Sala, A., Gandois, L., Gray, D.M., Hatcher, P.G., Honorio Coronado, E.N., Hughes, P.D.M., Huguet, A., Könönen, M., Laggoun-Défarge, F., Lähteenoja, O., Lamentowicz, M., Marchant, R., McClymont, E., Pontevedra-Pombal, X., Ponton, C., Pourmand, A., Rizzuti, A.M., Rochefort, L., Schellekens, J., De Vleeschouwer, F., Pancost, R.D., 2017b. Introducing global peat-specific temperature and pH calibrations based on brGDGT bacterial lipids. Geochimica et Cosmochimica Acta 208, 285–301. https://doi.org/10.1016/j.gca.2017.01.038.

Nott, C.J., Xie, S., Avsejs, L.A., Maddy, D., Chambers, F.M., Evershed, R.P., 2000. n-Alkane distributions in ombrotrophic mires as indicators of vegetation change related to climatic variation. Organic Geochemistry 31, 231–235. https://doi.org/10.1016/S0146-6380(99)00153-9.

Retallack, G.J., 2007. Cenozoic paleoclimate on land in North America. Journal of Geology 115, 271–294. https://doi.org/10.1086/512753.

Retallack, G.J., Orr, W.N., Prothero, D.R., Duncan, R.A., Kester, P.R., Ambers, C.P., 2004. Eocene-Oligocene extinction and paleoclimatic change near Eugene, Oregon. Bulletin of the Geological Society of America 116, 817–839. https://doi.org/10.1130/B25281.1.

Sheldon, N.D., Costa, E., Cabrera, L., Garcés, M., 2012. Continental Climatic and Weathering Response to the Eocene-Oligocene Transition. The Journal of Geology 120, 227–236. https://doi.org/10.1086/663984.

Sheldon, N.D., Grimes, S.T., Hooker, J.J., Collinson, M.E., Bugler, M.J., Hren, M.T., Price, G.D., Sutton, P.A., 2016. Coupling of marine and continental oxygen isotope records during the Eocene-Oligocene transition. Geological Society of America Bulletin 128, 502–510. https://doi.org/10.1130/B31315.1.

Sinninghe Damsté, J.S., Hopmans, E.C., Pancost, R.D., Schouten, S., Geenevasen, J.A.J., 2000. Newly discovered non-isoprenoid glycerol dialkyl glycerol tetraether lipids in sediments. Chemical Communications 1683–1684. https://doi.org/10.1039/b004517i

Spicer, R.A., Bera, Subir, De Bera, Sreelekha, Spicer, T.E.V., Srivastava, G., Mehrotra, R., Mehrotra, N., Yang, J., 2011. Why do foliar physiognomic climate estimates sometimes differ from those observed? Insights from taphonomic information loss and a CLAMP case study from the Ganges Delta. Palaeogeography, Palaeoclimatology, Palaeoecology 302, 381–395. https://doi.org/10.1016/j.palaeo.2011.01.024.

Spicer, R.A., Su, T., Valdes, P.J., Farnsworth, A., Wu, F.-X., Shi, G., Spicer, T.E.V., Zhou, Z., 2020a. Why 'the uplift of the Tibetan Plateau' is a myth? National Science Review. https://doi.org/10.1093/nsr/nwaa091.

Spicer, R.A., Valdes, P., Hughes, A., Yang, J., Spicer, T., Herman, A., Farnsworth, A., 2020b. New insights into the thermal regime and hydrodynamics of the early Late Cretaceous Arctic. Geological Magazine 157, 1729–1746. https://doi.org/10.1017/S0016756819000463.

Steinthorsdottir, M., Porter, A.S., Holohan, A., Kunzmann, L., Collinson, M., Mcelwain, J.C., 2016. Fossil plant stomata indicate decreasing atmospheric CO_2 prior to the Eocene-Oligocene boundary. Clim. Past 12, 439–454. https://doi.org/10.5194/cp-12-439-2016.

Su, T., Farnsworth, A., Spicer, R.A., Huang, J., Wu, F.-X., Liu, J., Li, S.-H., Xing, Y.-W., Huang, Y.-J., Deng, W.-Y.-D., Tang, H., Xu, C.-L., Zhao, F., Srivastava, G., Valdes, P.J., Deng, T., Zhou, Z.-K., 2019a. No high Tibetan Plateau until the Neogene. Science Advances 5, eaav2189. https://doi.org/10.1126/sciadv.aav2189.

Su, T., Spicer, R.A., Li, S.F.S.H., Xu, H., Huang, J., Sherlock, S., Huang, Y.J., Li, S.F.S.H., Wang, L., Jia, L.B., Deng, W.Y.D., Liu, J., Deng, C.L., Zhang, S.T., Valdes, P.J., Zhou, Z.K., 2019b. Uplift, climate and biotic changes at the Eocene-Oligocene transition in south-eastern Tibet. National Science Review 6, 495–504. https://doi.org/10.1093/nsr/nwy062.

Su, T., Spicer, R.A., Wu, F.-X., Farnsworth, A., Huang, J., Del Rio, C., Deng, T., Ding, L., Deng, W.-Y.-D., Huang, Y.-J., Hughes, A., Jia, L.-B., Jin, J.-H., Li, S.-F., Liang, S.-Q., Liu, J., Liu, X.-Y., Sherlock, S., Spicer, T., Srivastava, G., Tang, H., Valdes, P., Wang, T.-X., Widdowson, M., Wu, M.-X., Xing, Y.-W., Xu, C.-L., Yang, J., Zhang, C., Zhang, S.-T., Zhang, X.-W., Zhao, F., Zhou, Z.-K., 2020. A Middle Eocene lowland humid subtropical “Shangri-La” ecosystem in central Tibet. Proceedings of the National Academy of Sciences 202012647. https://doi.org/10.1073/pnas.2012647117.

Valdes, P.J., Armstrong, E., Badger, M.P.S., Bradshaw, C.D., Bragg, F., Crucifix, M., Davies-Barnard, T., Day, J.J., Farnsworth, A., Gordon, C., Hopcroft, P.O., Kennedy-Asser, A.T., Lord, N.S., Lunt, D.J., Marzocchi, A., Parry, L.M., Pope, V., Roberts, W.H.G., Stone, E.J., Tourte, G.J.L., Williams, J.H.T., 2017. The BRIDGE HadCM3 family of climate models: HadCM3@Bristol v1.0. Geosci. Model Dev 10, 3715–3743. https://doi.org/10.5194/gmd-10-3715-2017.

Weijers, J.W.H.H., Bernhardt, B., Peterse, F., Werne, J.P., Dungait, J.A.J., Schouten, S., Sinninghe Damsté, J.S., 2011. Absence of seasonal patterns in MBT-CBT indices in mid-latitude soils. Geochimica et Cosmochimica Acta 75, 3179–3190. https://doi.org/10.1016/j.gca.2011.03.015.

Weijers, J.W.H.H., Schouten, S., Sluijs, A., Brinkhuis, H., Sinninghe Damsté, J.S., 2007. Warm arctic continents during the Palaeocene–Eocene thermal maximum. Earth and Planetary Science Letters 261, 230–238. https://doi.org/10.1016/j.epsl.2007.06.033

Westerhold, T., Marwan, N., Drury, A.J., Liebrand, D., Agnini, C., Anagnostou, E., Barnet, J.S.K., Bohaty, S.M., De Vleeschouwer, D., Florindo, F., Frederichs, T., Hodell, D.A., Holbourn, A.E., Kroon, D., Lauretano, V., Littler, K., Lourens, L.J., Lyle, M., Pälike, H., Röhl, U., Tian, J., Wilkens, R.H., Wilson, P.A., Zachos, J.C., 2020. An astronomically dated record of Earth’s climate and its predictability over the last 66 million years, Science. American Association for the Advancement of Science. https://doi.org/10.1126/science.aba6853.

Witkowski, C. R., Weijers, J. W. H., Blais, B., Schouten, S., Sinninghe Damsté, J. S.: Molecular fossils from phytoplankton reveal secular pCO2 trend over the Phanerozoic, Sci. Adv., 4, eaat4556, 2018.

Wolfe, J.A., 1993. A method of obtaining climatic parameters from leaf assemblages. US Geological Survey Bulletin 2040.

Xu, J.-X., Ferguson, D.K., Li, C. Sen, Wang, Y.F., 2008. Late Miocene vegetation and climate of the Lühe region in Yunnan, southwestern China. Review of Palaeobotany and Palynology 148, 36–59. https://doi.org/10.1016/j.revpalbo.2007.08.004.

Yang, J., Spicer, R.A., Spicer, T.E.V., Li, C. Sen, 2011. “CLAMP Online”: A new web-based palaeoclimate tool and its application to the terrestrial Paleogene and Neogene of North America. Palaeobiodiversity and Palaeoenvironments 91, 163–183. https://doi.org/10.1007/s12549-011-0056-2.

Yi, T.M., Li, C. Sen, Xu, J.-X., 2003. Late Miocene woods of Taxodiaceae from Yunnan, China. Acta botanica Sinica 53, 1689–1699. https://doi.org/10.1017/CBO9781107415324.004.

Zanazzi, A., Kohn, M.J., Macfadden, B.J., Terry, D.O., 2007. Large temperature drop across the Eocene–Oligocene transition in central North America. Nature 445, 639–642. https://doi.org/10.1038/nature05551.

Zhang, Y., Ferguson, D.K., Ablaev, A.G., Wang, Y., Li, C., Xie, L., 2007. Equisetum cf. pratense (Equisetaceae) from the Miocene of Yunnan in Southwestern China and Its Paleoecological Implications. Internation Journal of Plant Science 168.

Tables

Table 1. Asian regional impact: Climate model simulations (Sim.) with Eocene (Priabonian) and Oligocene (Chattian) boundary conditions are used to test the response of pCO_2 and Tibetan topography configuration on temperature and precipitation. Green indicates which parameters are included in the simulation. pCO_2 is represented as either a change from 4x to 2x pre-industrial pCO_2 or no change in pCO_2, and Tibetan topography configuration is represented as only a valley, as only a plateau, or as a change from valley to plateau (Val-to-Plat). The response is shown as change in mean annual temperature (ΔMAT, °C) and change in mean annual precipitation (ΔMAP, mm/yr).

Sim.	pCO_2	Valley	Plateau	Val-to-Plat	ΔMAT	ΔMAP
1	4x to 2x	Yes	No	No	-6.0	150
2	Change	No	Yes	No	-6.0	198
3	Change	No	No	Yes	-6.2	182
4	No change	Yes	No	No	1.4	167
5	No change	No	Yes	No	1.7	173
6	No change	No	No	Yes	1.2	199

Table 2. Climate model simulations at different Tibetan topography (valley or plateau) for Lühe Basin during the Chattian. Conditions: 2x pre-industrial pCO_2 (560 ppm), latitude and longitude (21.1, 101.2), rotated latitude and longitude (29.9, 96.9). Abbreviations: experiment code (expt.), terrestrial lapse rate (Terr-Lapse), mean annual temperature (MAT, °C), warm-month mean temperature (WMMT, °C), cold-month mean temperature (CMMT, °C), and mean annual precipitation (MAP, mm/yr).

Tibetan topography	expt	Terr-Lapse	MAT	WMMT	CMMT	MAP
2.5 km valley	tfgkb	3.67	19.0	24.8	12.12	2.63
4.5 km plateau	tfgkd	4.83	18.9	24.5	12.15	2.73

Table 3. CLAMP climate estimates based on the Lühe town section leaf flora and analysed using the PhysgAsia2/Worldclim2 calibration. For more details on these metrics and how they are obtained see (Spicer et al., 2020b). Row 1: Temperature-related parameters: mean annual air temperature (MAAT, °C); warm month mean air temperature (WMMAT, °C); cold month mean air temperature (CMMAT, °C); mean minimum temperature of the warmest month (MinT.W, °C); mean maximum temperature of the coldest month (MaxT.C, °C). Row 2: Vapour pressure deficit parameters: mean annual vapour pressure deficit (VPD.ann, hPa); mean winter vapour pressure deficit (VPD.win, hPa); mean spring vapour pressure deficit (VPD.spr, hPa); summer vapour pressure deficit (VPD.sum, hPa); autumn vapour pressure deficit (VPD.aut, hPa). Row 3: Precipitation and evapotranspiration-related parameters: precipitation during the three consecutive wettest months (3-Wet, cm); precipitation during the three consecutive driest months (3-Dry, cm); mean annual potential evapotranspiration (PET.ann, mm); mean monthly potential evapotranspiration during the warmest quarter (PET.wrm, mm); mean monthly potential evapotranspiration during the coldest quarter (PET.cld, mm). Row 4: Humidity and enthalpy-related parameters: relative humidity (RH, %); specific humidity (SH, g/kg); moist enthalpy (Enth, kJ/kg); thermicity i.e. a measure of cumulative heat (Therm). Row 5: Growth-related parameters: length of the growing season i.e. time when the mean temperature is > 10°C (LGS, months), growing degree days > 0°C (GDD0); growing degree days > 5°C (GDD5); growing season precipitation (GSP, cm); mean monthly growing season precipitation (MMGSP, cm).

Temperature-related parameters				
MAAT (°C)	**WMMAT (°C)**	**CMMAT (°C)**	**MinT.W (°C)**	**MaxT.C (°C)**
15.9±2.4	26.8±2.9	4.6±3.5	23±2.9	10.4±3.5
Vapour pressure deficit parameters				
VPD.ann (hPa)	**VPD.win (hPa)**	**VPD.spr (hPa)**	**VPD.sum (hPa)**	**VPD.aut (hPa)**
6±2.4	3.2±1.5	4.7±4	8.7±3.5	7.4±2
Precipitation and evapotranspiration-related parameters				
3-Wet (cm)	**3-Dry (cm)**	**PET.ann (mm)**	**PET.cld (mm)**	**PET.wrm (mm)**
111±40	35±10	1002±166	27.5±14	125±24.5
Humidity and enthalpy-related parameters				
RH (%)	**SH (g/kg)**	**Enth (kJ/kg)**		**Therm (°C)**
65±10	8.3±1.8	321±0.8		295±75
Growth-related parameters				
LGS (month)	**GSP (cm)**	**MMGSP (cm)**	**GDD0**	**GDD5**
9.8±1.1	225±64	24±7	677±118	735±106

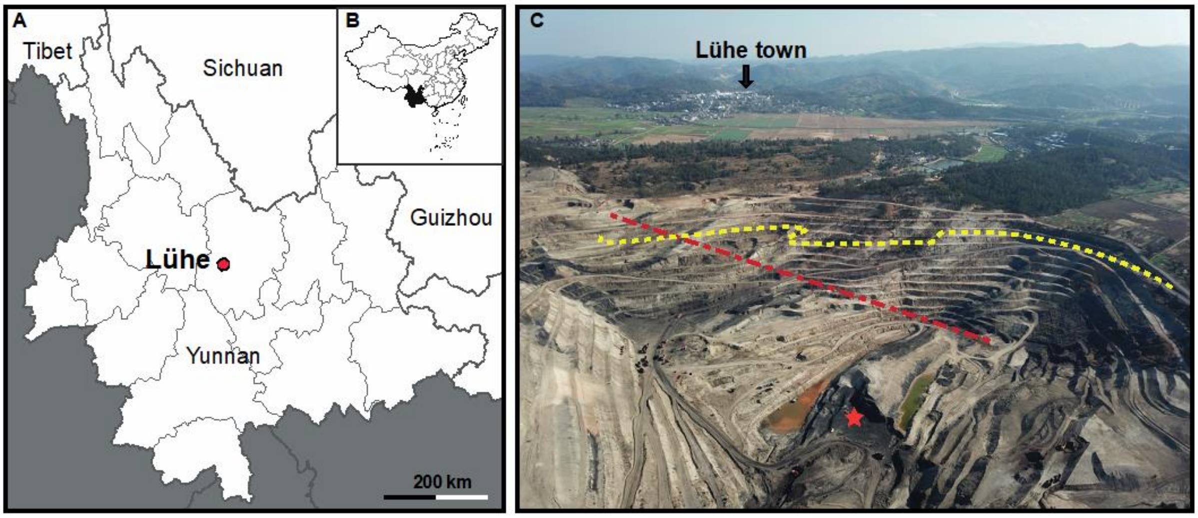

Fig. 1. Location and overview of the Lühe coal mine section. A-B: Location map (25°10′N, 101°22′E). C. Photograph of Lühe coalmine (yellow line indicated the sampling log of this study, red indicates the section logged by Li et al., 2020).

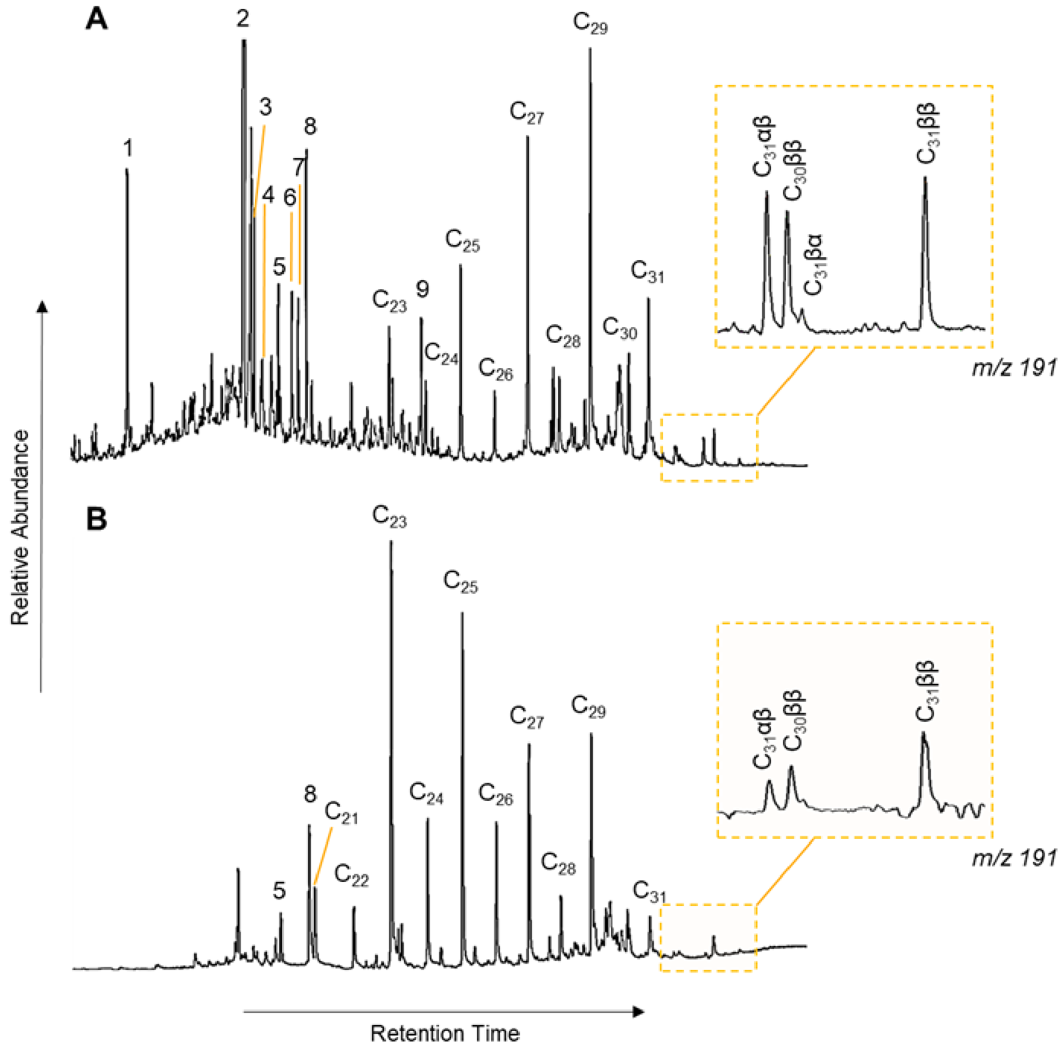

Fig. 2: Total ion chromatograms of the apolar fraction. A) Depth from base 268.0 m with high content of terpenoids and *n*-alkanes exemplary of the section, especially the C_{29} *n*-alkane dominance. B) Depth from base 58.5 m exemplary of the two outliers with C_{23} and C_{25} *n*-alkane dominance. Numbers represent: 1. Cadalene, 2. Norpimerane, 3. 18-norbietane, 4. 18-norabieta-8,11,13-triene, 5. Dehydroabietane, 6. 10,18-Bisnorabieta-5,7,9(10),11,13-pentaene, 7. Naphtalene, 8. Simonellite, 9. Tetramethyl-octahydrochrysene. Gold boxes zoom in on m/z 191 i.e., hopanes used for the thermal maturity index.

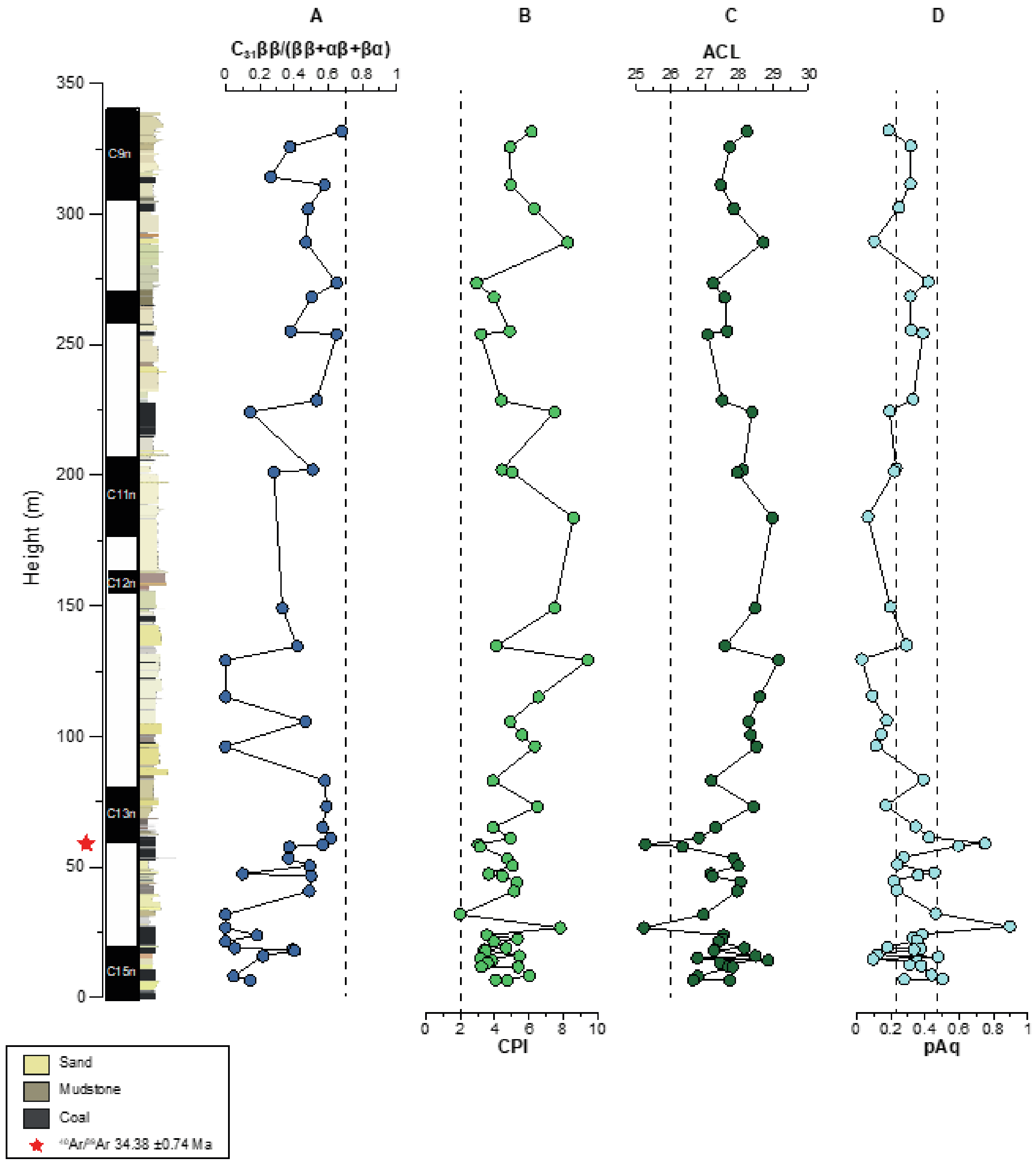

Fig. 3. Apolar biomarker indices for thermal maturity, vegetation, and environmental reconstructions. A) C_{31} hopane configuration ratio, B) Carbon preference index (CPI), C) Average chain length (ACL), and D) *P*-aqueous ratio (P_{aq}) which shows terrestrial versus aquatic input. Dotted lines: A) and B) limits for thermal maturity (C_{31} hopane ratio > 0.6, CPI < 2.0), C) terrestrial higher plants (ACL > 26), and D) terrestrial plant waxes ($_{aq}$ < 0.23) and submerged and floating macrophytes (P_{aq} > 0.48) (see text).

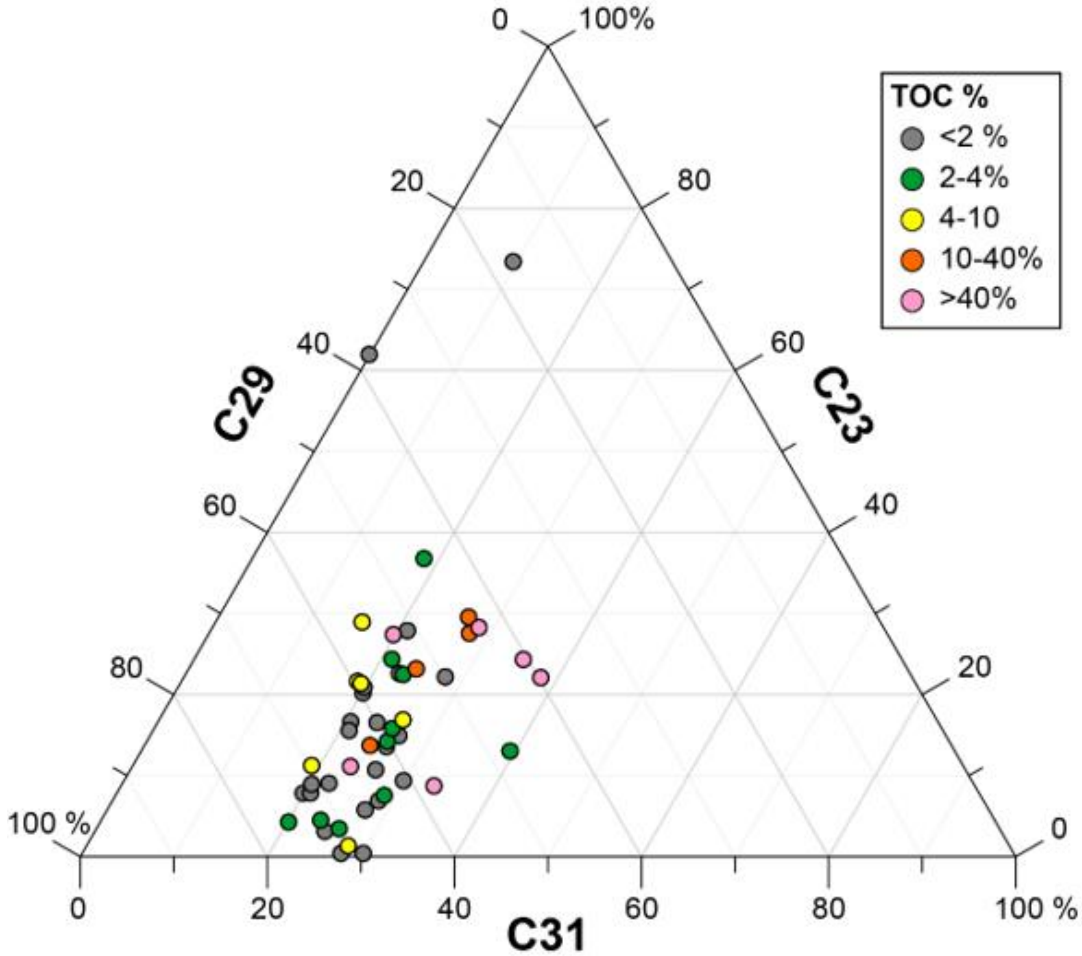

Fig. 4: Ternary plots of diagnostic *n*-alkanes. The relative percentage of C_{23}, C_{29}, and C_{31} *n*-alkanes in samples, differentiated based on their total organic content (TOC, %).

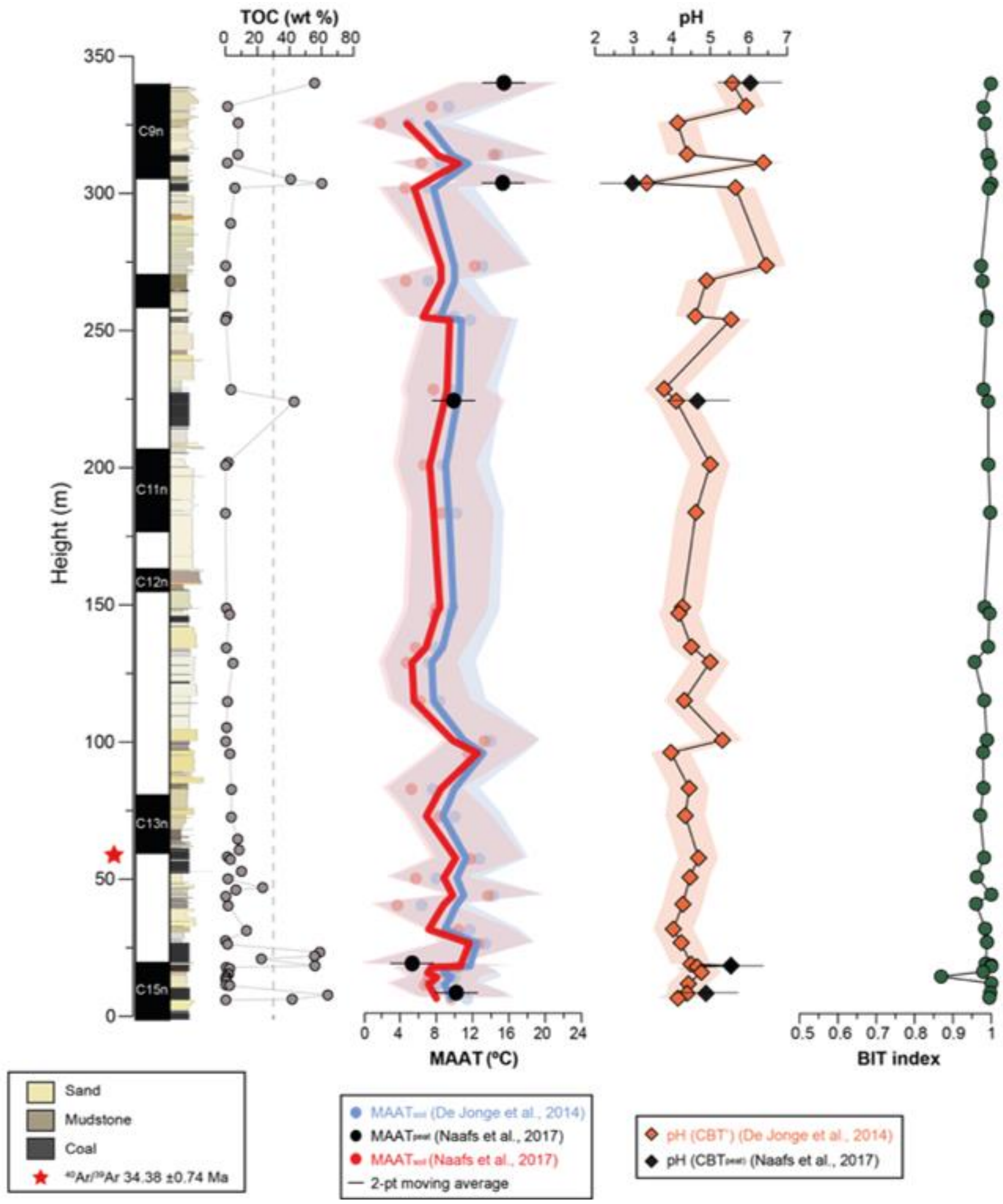

Fig. 5. TOC% and GDGT-derived proxies at Lühe coalmine: Total organic content (TOC %) for each analysed sample was used to constraint organic content and differentiate lignite samples (TOC > 30%). $MAAT_{soil}$ (mean annual air temperatures) and pH following: two soil calibrations in purple (De Jonge et al., 2014; Naafs et al., 2017a) and the peat-specific calibration in black (Naafs et al., 2017b) and Branched and Isoprenoid Tetraether (BIT) index (Hopmans et al., 2004).

Supplementary material

Methods

TOC (wt %) analyses

Total Organic Carbon (TOC) was determined on 56 samples using an Elementar vario PYRO cube at the University of Bristol, analysing C/N/S via catalytic combustion/reduction (1150 °C), optimised for coupling with an Isoprime IRMS for simultaneous determination of stable isotope ratios of C and N. Detection limits are at 0.001% or 10 ppm for C/N/S. An NC Soil reference standard was used to determine analytical precision. Prior to the analyses, all samples were prepared through an acid pre-treatment for carbonate removal, following the method by Hedges and Stern (1984).

Lipid extraction

For 56 samples from the Lühe coalmine section, 5 g of freeze-dried homogenised sediment were extracted using an Ethos Ex microwave extraction system with 20 ml of dichloromethane (DCM) and methanol (MeOH) (9:1 v/v). Microwave extractions were set using a 10-minute ramp to 70°C (1000W), a 10-minute hold at 70°C (1000W), and 20-minute cooling. Samples were then centrifuged at 1700 revolutions per minute (rpm) for 5 min to promote extract and sediment separation. Supernatants were removed and collected, and about 10 mL of DCM:MeOH (9:1 v/v) was added to the remaining sample and centrifuged again, before combining the available supernatants. This procedure was repeated up to five times to maximise lipid extraction. Elemental sulphur was removed by the addition of activated copper to the total lipid extract (TLE), left overnight. The TLE was concentrated by rota-evaporation and washed through a 4-cm sodium sulphate column using DCM:MeOH (9:1, v/v) to remove sediment particles. Subsequently, the TLE was split in two aliquots, and one of these was separated over a 4-cm alumina column by elution in an apolar fraction using hexane:DCM (9:1 v/v, 5 ml), and a polar fraction using DCM:MeOH (1:2 v/v, 4 ml). The apolar fraction was re-dissolved in hexane and analysed by GC-MS. The polar fraction was re-dissolved in hexane:isopropanol (99:1, v/v) and passed through a 0.45 μm polytetrafluoroethylene filter before analyses by HPLC-MS.

GC-MS

Apolar fractions were analysed at the University of Bristol using a Thermo Scientific ISQ Single Quadruple gas chromatography mass spectrometry (GC-MS) system, fitted with a fused HP-1 silica capillary column (50 m x 0.32 mm i.d., 0.17μm film diameter). Using helium as the carrier gas, 1 μL of sample dissolved in hexane was injected at 70 ℃ using an on-column PTV injector in splitless mode. The temperature program was set to four stages: 70 ℃ hold for 1 min, ramping to 130 ℃ at 20 ℃/min, then ramping to 300 ℃ at 4 ℃/min, and finally holding 300 ℃ for 20 min. The electron ionisation (EI) source was set at 70 eV. The emission current was set to 150 μA and scanning occurred between *m/z* ranges of 50-650 Daltons in full scan mode. The instrument accuracy was determined using an external fatty acid methyl ester (FAME) standard. Compound identification was carried out based on published spectra, characteristic mass fragments, and retention times.

HPLC-MS

Filtered polar fractions were analysed by high performance liquid chromatography/atmospheric pressure chemical ionisation – mass spectrometry (HPLC/APCI-MS), using a ThermoFisher Scientific Accela Quantum Access Triple quadrupole MS at the University of Bristol. Normal phase separation was achieved using two Waters Acquity UPLC BEH Hilic columns (2.1×150 mm; 1.7 μm i.d.) with a flow rate of 0.2 ml min^{-1}, following the method by Hopmans et al. (2016). Samples were eluted using a linear gradient of hexane hexane:IPA (9:1, v/v) (Hopmans et al., 2016), from an injection volume of 15 μL, out of 100 μL. Analyses were performed using selective ion monitoring mode (SIM) to increase sensitivity and reproducibility (*m/z* 1302, 1300, 1298, 1296, 1294, 1292, 1050, 1048, 1046, 1036, 1034, 1032, 1022, 1020, 1018, 744, and 653), and $M + H^+$ (protonated molecular ion) GDGT peaks were manually integrated.

Supplement references

Hopmans, E.C., Schouten, S., Sinninghe Damsté, J.S., 2016. The effect of improved chromatography on GDGT-based palaeoproxies. Organic Geochemistry 93, 1–6. https://doi.org/10.1016/j.orggeochem.2015.12.006.

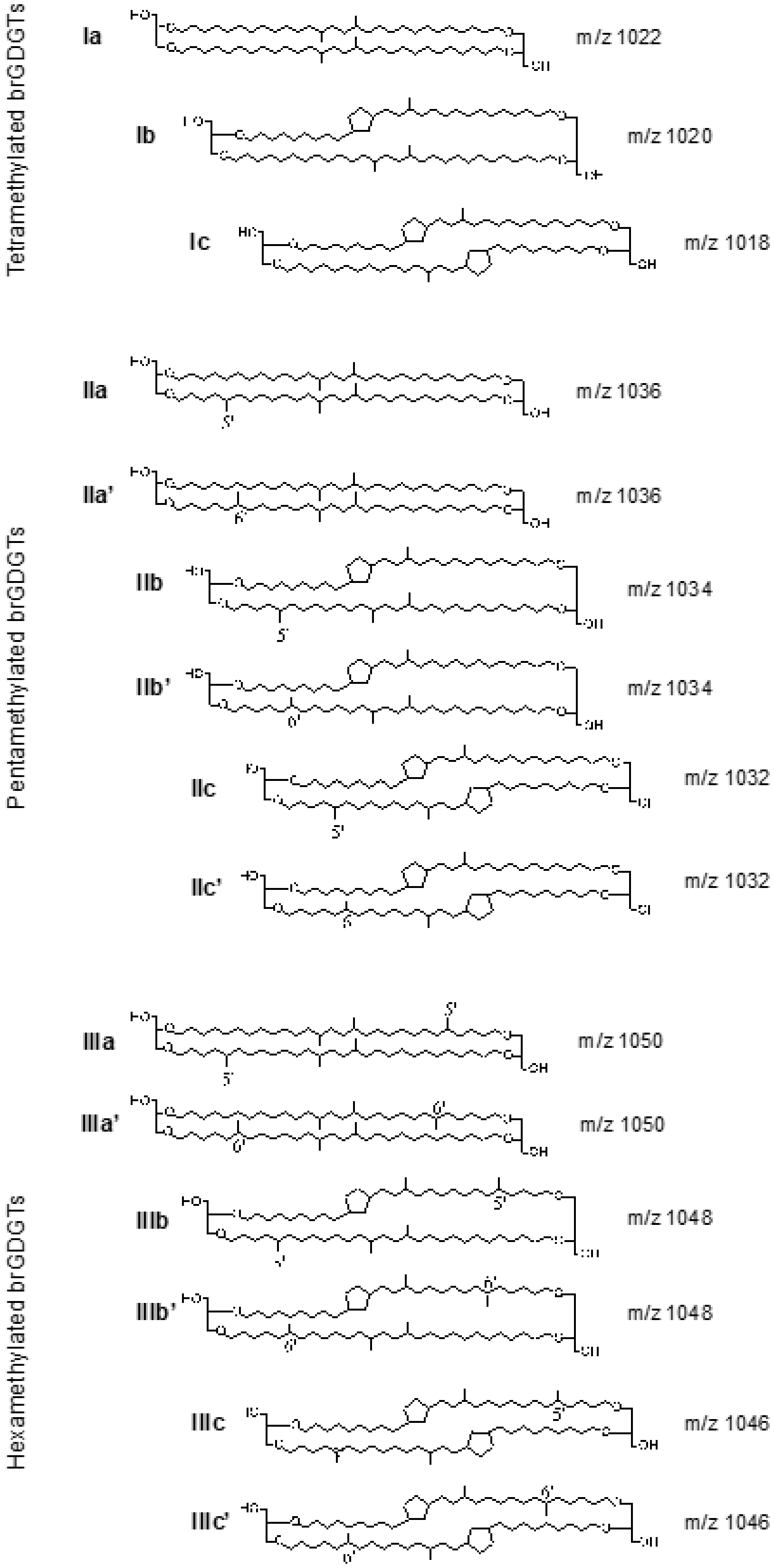

Fig. S1. Structures of brGDGTs, as discussed in the text.